Colloid and Polymer Science (2024) 302:103–115
https://doi.org/10.1007/s00396-023-05177-z

RESEARCH

A facile preparation of biochar-anchored magnetic photocatalytic PVDF composite for water remediation

Huseyin Gumus[1] · **Bülent Büyükkıdan**[2]

Received: 1 June 2023 / Revised: 15 September 2023 / Accepted: 28 September 2023 / Published online: 13 October 2023

Abstract

A magnetic photocatalyst composite was obtained with an environmentally friendly approach. Controlled carbonized wastes that cannot be reused as textile materials with polymeric matrix were added to the polymeric support. The carbonization behaviors and physical properties of polymeric composites were investigated by thermal analysis, Fourier transform infrared spectroscopy, X-ray diffractometer, and transmission and scanning electron microscope analysis. Photocatalytic dye removal performances of composites were investigated in batch medium (at 25 °C and 10–150 mg/L methyl orange model pollutant). The $FeCl_2.4H_2O$-impregnated waste sample was carbonized at 350 °C, whereas this value is 400 °C for non-chemical activated samples. The biochar gained magnetic feature due to the formation of Fe_3O_4 crystals confirmed in diffraction patterns. Catalytic Fe-biochar prepared in a single step in a controlled manner stabilized polyvinylidene fluoride structure by phase inversion. The dye removal efficiency of the composite was investigated. Fe-biochar-PVDF composite exhibited 97.4% dye conversion under 254 nm, 30 W ultraviolet light for 30 min. It is a good example for the importance of waste recycling and the production of fine materials under low-cost conditions. Fe-biochar-PVDF composites are promising materials for use as self-cleaning membrane material in filtration systems.

Keywords Magnetic biochar · Carbonization · Photocatalysis · Environmental protection · Waste recycling

Introduction

Iron salts are frequently used modification agents for magnetic biochar preparation due to their advantages of heavy metal removal and organic matter degradation. In addition to catalyzing some reactions, the magnetic feature facilitates the easy separation of the catalyst from the reaction medium [1].

Thanks to the functional groups, the magnetic $MnFe_3O_4$-corn straw composite showed 154.94 mg/g Pb(II) and 127.83 mg/g Cd(II) removal performance from water [2]. The biochar obtained by the pyrolysis of waste sugar in N_2 atmosphere was treated with $FeSO_4$ and $FeCl_3$ according to the precipitation method. The prepared magnetic biochar (Mag-BCNP) adsorbed 50.24 mg/g 17B-estradiol [3]. Uranium (VI) removal performances of watermelon magnetized rinds-based biochar and normal biochar were compared in an electromagnetic semi-batch column. The results were reported as 323.56 and 135.86 mg/g, respectively [4]. Magnetic biochar is frequently applied in the removal of organic impurities. The 2,4-Dichlorophenol (2.4-DCP) and atrazine removal performance of Fe_3O_4-biochar was recorded as 298.12 mg/g and 102.17 mg/g, respectively [5]. Magnetic biochar prepared by K_2FeO_4 treatment of pyrolyzed jackfruit peel at 300 °C presented 61.30 mg/g, 129.61 mg/g, and 1238.30 mg/g Cu^{2+}, methylene blue (MB), and malachite green (MG) adsorption [6].

Highlight
- Magnetic photocatalytic composites were prepared by the addition of magnetic biochar obtained from waste textile remnants.
- The waste recycling provided environmental protection and fine material production at low temperatures.
- Chemical activation reduced the temperature of carbonization process by inducing the decomposition of polymeric matrix.

✉ Huseyin Gumus
huseyin.gumus@bilecik.edu.tr

Bülent Büyükkıdan
bulent.buyukkidan@dpu.edu.tr

[1] Osmaneli Vocational School, Bilecik Seyh Edebali University, 11500, Osmaneli, Bilecik, Turkey

[2] Department of Chemistry, Kutahya Dumlupinar University, Kutahya, Turkey

Taking impurities from the aqueous medium by adsorption and confining them to the solid surface does not provide a final purification in some cases. Problems such as clogging of the adsorbent surface and reduced reuse efficiency may occur. Magnetic biochar can form radicals by the interaction of oxygen-rich groups. These active groups can interact with organic soils and break these structures. At the same time, it can be easily separated from the environment with a magnet have been used as an advanced pollution removal. One hundred milligrams of Fe_2TiO_5-modified biochar (Fe_2TiO_5/BC) was used for photocatalytic removal of methylene blue at 365 nm 100 W UV radiation [7]. Degradation took place through MB adsorption on biochar through effective reactive oxygen groups inducting photo-fenton reaction. Tetracycline oxidation with sulfate radicals was achieved by persulfate activation [8]. Rhodamine B (Rb) oxidation with the presence of chitin biochar-$ZnFe_2O$ was conducted. Hydroxide radicals formed as a result of the activation of hydrogen peroxide-interacted Rb [9]. The oxidation of methyl orange (MO), methyl red (MR), and methylene blue (MB) was catalyzed by Ag-containing magnetic biochar dots (BCDs-Ag-MNPs) in the presence of $NaBH_4$. Those are examples of applications where magnetic biochar is used as a catalyst [10].

Magnetic biochar in various compositions was used for the oxidation of impurities. It has been modified with iron derivatives to facilitate reactions as electron transfer and/or electron donor. The magnetic additive on the adsorbents and catalysts was preferred for the reasons of gaining large surface area, well-dispersed pore structure, ability to absorb reactants, as well as easy separation from the reaction media and reusing the catalyst with high performance.

Magnetic-polymeric composites were also obtained by immobilization of magnetic structure on the polymer. Those were used as catalysts to purificate contaminated waters at the membrane form. Fe_3O_4/PVDF-HFP composite membrane exhibited 99.99% salt filtration performance thanks to its high solar absorption feature [11]. In addition to high chemical, thermal, and physical resistance, the polymer support is expected compatible to form homogeneous structure with the magnetic additive. Hydrophilic Fe_3O_4/(PVDF) three-channel hollow fiber catalytic membrane exhibited high water flow (175.8 L m^{-2} h^{-1}) and MB degradation (97%) efficiency [12]. Improvements in flow, antifouling, and filtration performances have been reported in Fe_3O_4–palygorskite/PVDF and Fe_3O_4@TiO_2 photocatalytic PVDF ultrafiltration membranes [13, 14]. Ag-interacted polydopamine-coated magnetic biochar (MC-PDA-Ac) showed 90% catalytic effect against MB, RhB, and MO organic impurities in the presence of NH_4 [15].

One of the most important parameters affecting the surface area, functional groups, and therefore efficiency of the activated carbon is the processing order. In the method where the carbon source is chemically activated beforehand, the type, amount, and impregnation time of the chemical greatly affect the properties of the final product. There are applications where activated carbon is obtained by applying only temperature as a parameter and then the desired modification is made.

Fe/AC and $LaFeO_3$/AC catalysts were prepared by adding commercial activated carbon to aqueous solutions of 10% $La(NO_3)_3$•$6H_2O$ and $Fe(NO_3)_3$•·$9H_2O$ salts for the remediation of pharmaceutical wastewater. Then it was evaporated at 80 °C and calcinated at 300 °C for 3 h [16]. For the preparation of the Fe/AC membrane, AC and $FeSO_4$·$7H_2O$ were mixed in 70 ml of distilled water and then kept in a hydrothermal reaction vessel at 100 °C for 24 h. The dried sample was calcinated at 800 °C for 2 h and fixed on the PES membrane surface by filtration [17]. The performance of the prepared composite was 99.92% for humic acid removal from water.

The studies focused on the preparation of activated carbon by heating a wide variety of biomass directly [18]. There is an important advantage of chemical activation of waste material before heating. The catalytic effect of some cations and metals may decrease the heating rate in addition to stimulating the formation of hydroxyl, amine, and carboxyl groups. Thus, the required energy for the conversion of the carbon source may decrease. For this reason, it is an economical and smart method to obtain biochar by modifying it with catalytic chemicals before heating. Fe and Fe oxide immobilized composite structures have advantages such as easy usability, separation from solution without requiring chemicals, and act of Fenton agent under radiation. Catalytic Fe/Ac-polymeric composites with increased surface area with activated carbon have been developed. However, Fe/AC-doped polymeric composites prepared in a single step by controlled burning of waste carbon sources with Fe derivatives have some advantages. These are environmentally protective and low-cost processes, mainly due to recycling. They are important alternatives to catalysts prepared using pure reagents.

According to our overview, preparation, and investigation of physical-photocatalytic properties of magnetic waste, textile-based biochar composites will be examined for the first time in this study. The carbonization behavior and effect of chemical activation on the waste textile with $FeCl_2.4H_2O$ were examined. Physical properties of magnetic composites were analyzed by XRD, FT-IR, TG, and SEM techniques. The best composition (polymer-additive) was determined in terms of the photocatalytic performances under UV light.

Materials and methods

Materials

Waste textile remnants (TX) consisting of 80% cotton and 20% polyester were obtained from Uşak organized industrial Zone, Turkey. Ethanol (C_2H_5OH, pure, ≥ 95%), sodium

hydroxide (NaOH, analytical grade, ≥ 98%), hydrochloric acid (HCl, analytical grade, ≥ 37%), and iron (II) chloride tetrahydrate ($FeCl_2.4H_2O$, reagent plus, ≥ 98%) were purchased from Sigma Aldrich and used without any processing. Polyvinylidene fluoride (PVDF, Solef 6010 from MINGER) was used as polymer matrix, and N,N-dimethylformamide (DMF, 73.09 g/mole, 0.944 g/mL, analytical grade, ≥ 99%, Sigma Aldrich) was solvent. Methyl orange (MO, 4-[4-(Dimethylamino)phenylazo]benzenesulfonic acid sodium salt) Double distilled water was used as phase separation and cleaning solution for catalytic Fe-CWT composites.

Preparation of Fb and PFb composites

The remnants (TX) that emerged from the textile industry and could not be reconsidered as the textile component was used as raw materials as active carbon raw materials. Those (TX) were washed with ethanol and hot water at approximately 70 °C to remove industrial grasses and dyes. After rinsing and dried at 60 °C for 24 h, 5 g TX was wetted with 25 ml activating $FeCl_2.4H_2O$ solution (Fe-TX), as applied in our former study [19]. The mass ratio of activating chemicals to TX was adjusted as 0.14–1.4–50 for 1–1.5 h activation time. Before carbonization, the furnace was cleaned by N_2 (3 mL/s) flow. Chemically modified samples were dried at 60 °C for 24 h, and those were carbonized at 350–400 °C in a muffle furnace with a 10–15 °C/min heating rate. Carbonized samples were weighted and grounded then they were passed through a 150-µm sieve. The biochar obtained by the carbonization of Fe-TX was called as Fe-biochar (Fb).

Fb-anchored composites (Fb-PVDF) were prepared by mixing of 1.6 g polymer in 10 mL DMF. Powder Fb prepared by the carbonization of 0.5 mol/L $FeCl_2.4H_2O$ treated TX was added at the 0, 5, 10, 15, and 20% mass ratio. The solution was stirred at 250 rpm for 2 h at 60 °C for homogeneous dispersion. After waiting for 10 min to avoid air bubbles, it was cast on to a glass plate (20 cm × 15 cm) by a 300-µm casting knife at 25 °C. The glass plate was quickly immersed into distilled water for phase inversion, and it was waited for 24 h. Flat sheet composites were stored in pH ≅ 9 distilled water to prevent contamination and drying. Samples were dried at 40 °C and cut into appropriate pieces according to the analysis procedure. Fb composites were called as P (for PFb-0, raw PVDF), PFb-5, PFb-10, and PFb-20 according to the mass ratio% of Fb versus polymer.

Characterization of Fb and PFb composites

Thermal stability of samples was analyzed by Seiko Exstar 7200 thermal analyzer (TG–DTA, at 30–900 °C temperatures with 10 °C/min heating rate). The crystallinity of powders and composites was investigated by X-ray diffractometer (XRD, Rigaku 2000) at 2θ:2–70° with 2°/min scanning speed. Powder and composite morphologies were imaged by scanning electron microscopy (SEM) at 10 kV (Carl Zeiss ULTRA Plus). For cross-section images of samples, those were firstly broken in liquid nitrogen to get a better angle. Then it was gold plated and fixed to the carbon holder. The distribution of activated carbon-Fe nanoparticles fixed on the PVDF support structure was imaged with a Hitachi H 7650 transmission electron microscope (TEM) at 100 keV. PFb polymeric composite was cut to 50 nm with a diamond blade, and slices were placed on a copper grid using a microtome.

Functional molecular groups were determined by Perkin Elmer Fourier transform infrared spectroscopy (FT-IR) over a range of 4000–400 cm^{-1}. The surface area of samples was measured by TriStar II 3020 Version 3.02 Brunauer–Emmett–Teller (BET) device. Water uptake capacity (WU%) of composites was determined to get information about water absorption and pore distribution with porosity% values. For this, composites stored in water were weighted (W_w) after mopping slightly with blotting paper. Wet membranes were dried in a 40 °C vacuum oven for 2 h, and these were weighed again (W_d). By using wet and dry weights of membranes, water uptake capacities were calculated by Eq. (1).

$$WU(\%) = \frac{W_w - W_d}{W_w} x100 \quad (1)$$

Porosity percentages of composites (PO%) were calculated by weight of wet and dry membranes [20] according to Eq. (2).

$$PO(\%) = \frac{W_w - W_d}{dA\delta} x100 \quad (2)$$

where d is the density of water used at 25 °C, A is membrane area in wet state (cm^2), and δ represents the thickness of membrane in wet form (cm).

Dye removal experiments by adsorption and photocatalytic effect

MO adsorption performances of composites were tested in a cylindrical flask. Temperature and pH of the solution were adjusted to 25–35 °C and pH ≅ 7.0 respectively by 0.05 mol/L HCl and NaOH.100 mL MO aqueous solution (10–150 mg/L), and 0.3 g adsorbent were stirred at 150 rpm for 75 min. In order to understand the dye removal performances by adsorption and photocatalytic effect, the adsorption and photocatalysis were examined sequentially. Adsorbents were separated by magnet, and the MO amount taken from the solution in 5 min was analyzed by a UV–vis spectrometer at 466 nm. As soon as each solution reached equilibrium, the process was continued until the second

reading value of the sample was the same as the first. It was exposed to 30 W (Philips, spectral range 254 nm) ultraviolet radiation at a distance of 15 cm for photocatalytic experiments. The residual MO value in the solution was recorded as the initial value for the catalytic reactions. The photocatalytic activity of each catalyst was determined under the UV radiation with air circulation for 30 min and in the presence of 5.10^{-5} mol/L H_2O_2 for 5 min sequentially. Composites were separated by magnet, and the MO samples taken at 5-min intervals were analyzed. Schematic representation is given at Fig. S1. Pseudo-first- and pseudo-second-order kinetic models were applied for MO removal with Langmuir and Freundlich isotherm models. Equations for adsorption kinetic and isotherms were given in Table S2.

The leaching of Fe from the photocatalyst to the solution medium was verified with the Agilent Technologies 240 FS AA spectrometer.

Result and discussion

Characterization of Fb and PFb composites

The biochar obtained by carbonization of 0.5 mol/L $FeCl_2.4H_2O$-treated TX was found to have the best composition. It presented physical and chemical uniformity. So, the biochar prepared at [05]-[Fe]-[1]-[350] conditions were preferred as an additive to obtain 0, 5, 10, and 20% PFb composites.

The thermal behaviors of the raw TX and $FeCl_2$-treated samples (Fe-TX) under the controlled heating are given in Fig. 1. The pyrolysis of the untreated TX sample in the range of 30–900 °C took place in three main stages. Evaporation and decomposition of very small amounts of moisture and volatile components up to 200–230 °C could be called as the first stage. An intense decomposition of the structure took place at around 230–600 °C with 95% mass loss. The small shoulder seen at 280 °C in the DTA curve of TX with the sharp exothermic peak at around 380 °C can be explained by the carbonization of cellulose derivatives (Fig. S2 and S3) [21]. Compared to TX, there is a clear difference in the TG curve of Fe-TX. The evaporation of moisture, volatile compounds, and the mass loss due to volatilization of the hydrated water in the $FeCl_2$ occurred in the first stage. Dehydration and evaporation of volatile compounds increased due to the catalytic effect of $FeCl_2$. The mass loss of Fe-TX at temperatures between 100 and 300 °C was approximately 3 times higher than that of TX. While the maximum decomposition of TX was recorded at 380 °C, this was 350 °C for Fe-TX. The thermal decomposition of the TX was completed at 605 °C with the combustion of the carbon content totally in the second stage. Small increases of Fe-TX mass% were due to Fe_3O_4 formation, and rapid mass loss is associated with dehydrochlorination and reduction of iron in the presence of carbon [22].

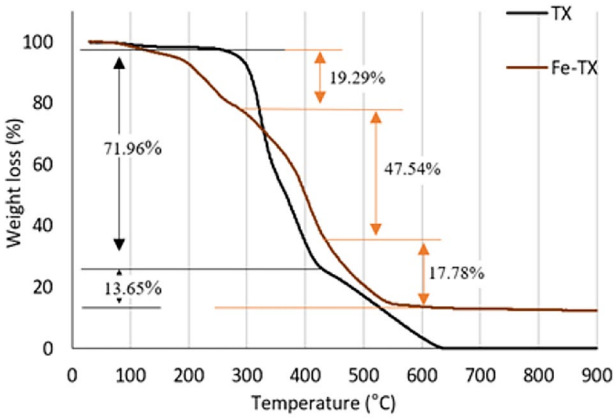

Fig. 1 TGA curves of TX and Fe-TX patterns

The thermal degradation of PFb composites with PVDF occurred mainly in 4 stages (Fig. 2 and Fig. S4–S6 for detailed explanation). It is understood that polymer degradation proceeded through the separation of CH and CF bonds up to 430 °C is similar for P, PFb-5, and PFb-10. The highest mass loss in the specified temperature range was recorded for the PFb-20 sample. The reason for that was the presence of catalytically effective components at the highest rate. Semi-combustion of PVDF was completed at 500 °C. On the other hand, an increase in the mass of the composites indicates the formation of iron oxides in the structure. The mass loss of PFb samples increased after 450 °C. Maximum decomposition temperatures (T_{max}) for P, PFb-5, and PFb-20 were recorded at 550 °C. That was recorded in a wide range covering 500–700 °C for PFb-10 and completed at 740 °C [23]. This can be explained by the controlled combustion of the organic structure thanks to proportional dispersion of the additive inside PFb-10. Homogeneity enabled the formation of new oxide structures. The combustion of the polymer in PFb-20 composite was completed approximately 40 °C earlier than the P and PFb-5 samples. Twenty percent additive provided a high catalytic effect in the completion phase of decomposition. On the other hand, it is understood from the thermal behaviors of P and PFb-5 that 5% additive ratio has an insufficient catalytic effect for thermal decomposition. The Fb acted as a catalytic magnetite, and it increased the efficiency for polymer decomposition.

X-ray diffraction patterns of Fb composites are shown in Fig. 3. The diffraction peaks at around 2theta = 36 and 42° of the composites indicate the presence of iron oxide structure [24]. Magnetite formation as a result of Fe activation of waste textiles was understood from the XRD diffraction pattern of Fb [25]. It was at around 2theta = 57 and 63° for PFb-20 composite. A small shift at magnetite peaks of composites proved the interaction between the biocarbon and the polymer chain. The solid-polymer interaction changed

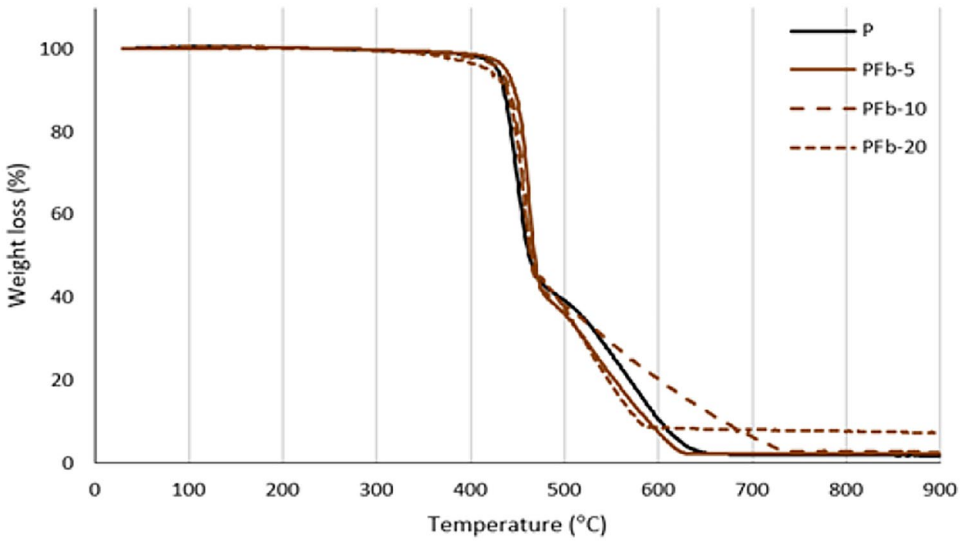

Fig. 2 TGA curves of P and PFb composites (Fig. S4–S6 for detail)

with the amount of additive added. The transformation of alpha phase of PVDF peaks at 18.56 and 20.1 into a single peak at 20.5 pointed out the formation of beta phase in PFb-5 [26, 27]. The change observed for 26.8 peak intensity indicates the interaction between the biochar and polymeric chain. The amorphous structure increased with the increase in magnetite-type biochar rate.

Morphological changes on the composite surfaces were investigated by SEM and TEM analysis (Fig. 4). Rough and semi-porous structure of the raw PVDF surface changed with increasing doping ratio. Partial agglomeration occurred due to the activated carbon in the structure of powder Fb. However, the uniform distribution of Fb on the polymer support can be seen from the TEM image of PFb. Roughly spherical Fb nanoparticles with an average diameter of 31 nm were homogeneously embedded in the polymer. That verifies that PVDF-Fb interaction facilitates the dispersion of nanoparticles. The 5% Fb-added structure (PFb-5) had relatively larger pores compared to the raw PVDF. That is the ideal ratio for the homogeneous distribution of the solid in the polymer. It can be considered as the preferred additive amount in filtration membranes, especially to obtain a high flow rate. However, a catalytically effective composite which contains maximum additives was aimed in this study. Also, additives were expected that will not impair the physical strength of the polymer and will not prevent substrate

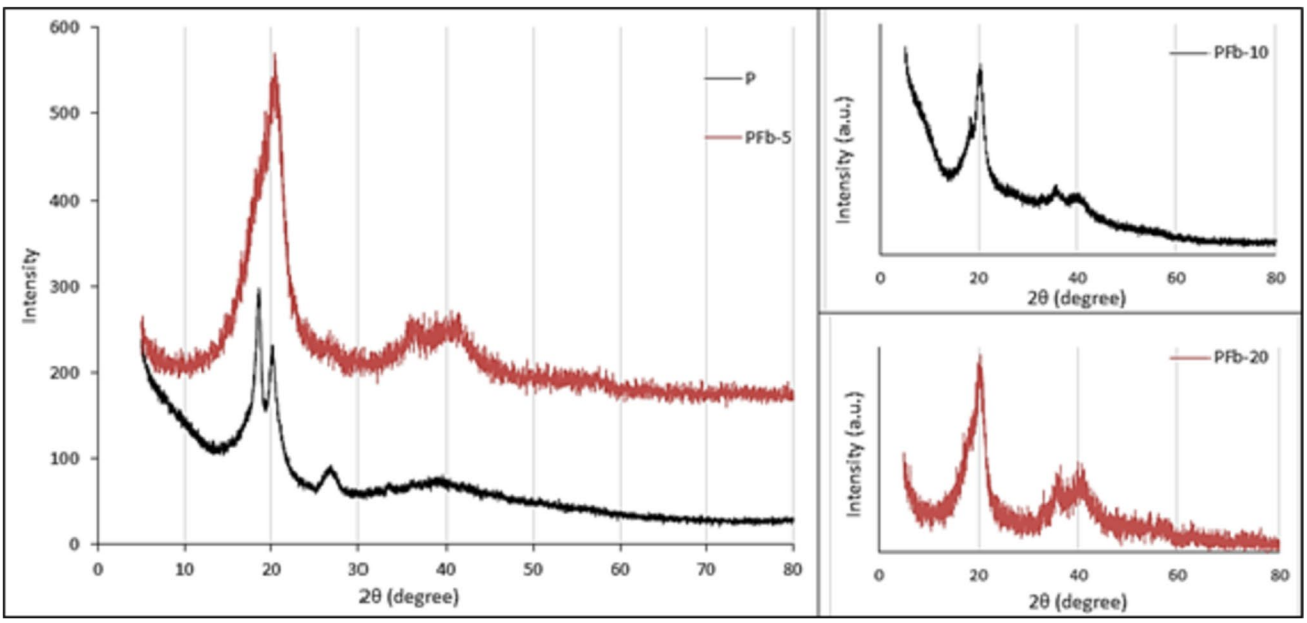

Fig. 3 XRD patterns of P and PFb composites

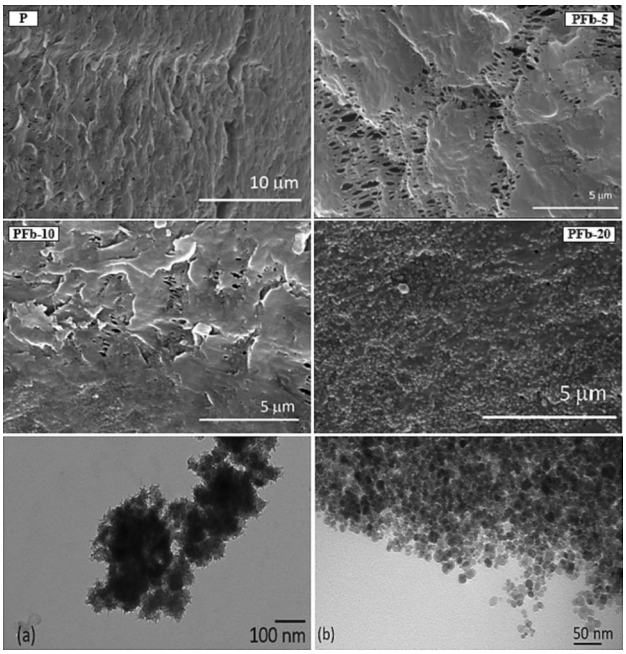

Fig. 4 SEM images of P and PFb composites with TEM images of Fb (**a**) and PFb-10 (**b**)

migration. Composite properties changed with increasing additive ratio in PFb-10 and PFb-20. This arrangement may have occurred as a milestone at any value between 5 and 10%. It was observed that PFb-10 composite surface had more compacted and narrower pores than raw PVDF. Also, Fb residues could be observed easily on the PFb-20 composite surface. As a result of the 20% additive, an impermeable structure was formed, and the pores on the surface of the composite were greatly narrowed. The usability and feasibility of PFb-20 and PFb-30 due to their high catalyst content were evaluated by considering WU%, PO%, and photocatalytic test results.

The interaction of Fb with PVDF and the molecular changes were analyzed by FT-IR (Fig. 5). The changes in the composite peaks at around 450–800 cm^{-1} were the results of the Fe–O stretching vibration [28]. The spectrum bands observed at around 1405 and 875–1178 cm^{-1} belong to the CH and CF_2 bond stretching vibrations of PVDF. The band at 1070 cm^{-1} corresponds to CF stretching vibration of composites obtained by Fb addition. A small shift of this band indicated that Fb contribution is effective in the formation of new structure. This is evidenced by the changes of peak strength on characteristic α-phase of 761, 796, and 975 cm^{-1} bands with and disappearances [29]. These changes are also pointed to the importance of the contribution ratio because different compositions created different changes in the same characteristic bands. The C=C and C=O and C–O–C interactions of Fb can be understood from the 1723, 1629, and 1092 cm^{-1} bands, respectively with the OH band of hydrate derivatives at 3023 cm^{-1} [19, 25]. The 1051 and 823 cm^{-1} bands recorded in the Fb structure correspond to the Fe–O interactions. In addition, IR spectra of raw waste textile (TX) and Fe-impregnated (Fe-TX) samples were also shared (Fig. S7–S8) to fully understand the effect of Fe activation. It is understood from the change of metal oxide bands at the range of 800–450 cm^{-1} with a single peak at 1620 cm^{-1} that even Fe activation was effective before carbonization. The emerging of metal oxide-induced bands and new phase formations in the polymer chain are the result of Fe activation [30].

The surface area of samples (BET results) was presented with wettability WU% and porosity PO% data to better understand the change in surface area (Table 1). The ideal surface area for polymers and composites has been achieved. The composite surface after the Fb addition partially shrank and became compressed with an increasing Fb ratio. A remarkable change was obtained in the PFb-10 sample with a surface area of 12.35 m^2/g compared to P (4.11 m^2/g). The pore width of PFb composites were smaller than P and did not change much with increasing Fb ratio. Total pore volumes of composites generally decreased related to micropores. However, the increase in the surface area, WU% and PO% values for PFb-10 indicate the formation of many small pores in the pressed structure (PFb-20). Numerous small pores on the filtration composites have structural and functional advantages in some cases. Small pores ensure the preservation of physical resistance with higher filtration and catalysis efficiency of small-sized substrate molecules. On the other hand, it can cause rapid clogging or the inability of large molecules to reach the active areas [31].

The decrease in surface area of PFb-20 composite can be directly explained by compressed structure due to increased Fb ratio. Ideal pores were formed, but due to the abundance of Fb, these pores were filled with Fb particles, resulting in a low surface area. The water permeation performances of structures (WU%) varied proportional to the pore volume and PO%. Thanks to its large number of small pores, the best water uptake capacity of 66.5% was obtained with PFb-10. Despite the larger pore volume and pore structure, the low values of PFb-20 may be due to the compacted structure and water repulsion of Fb. Additive ratio is highly effective in the adjustment of composite properties.

Dye removal by adsorption and photocatalysis

Adsorption properties

It was investigated whether the dye removal of the composites was by adsorption or photocatalysis. For this, 100 mL (10–150 mg/L) MO aqueous solution and 0.3 g composite were put into an adsorption flask. The mixture was stirred at 150 rpm for 75 min. The solution acidity was adjusted to 7, which was approximately the initial pH value, considering

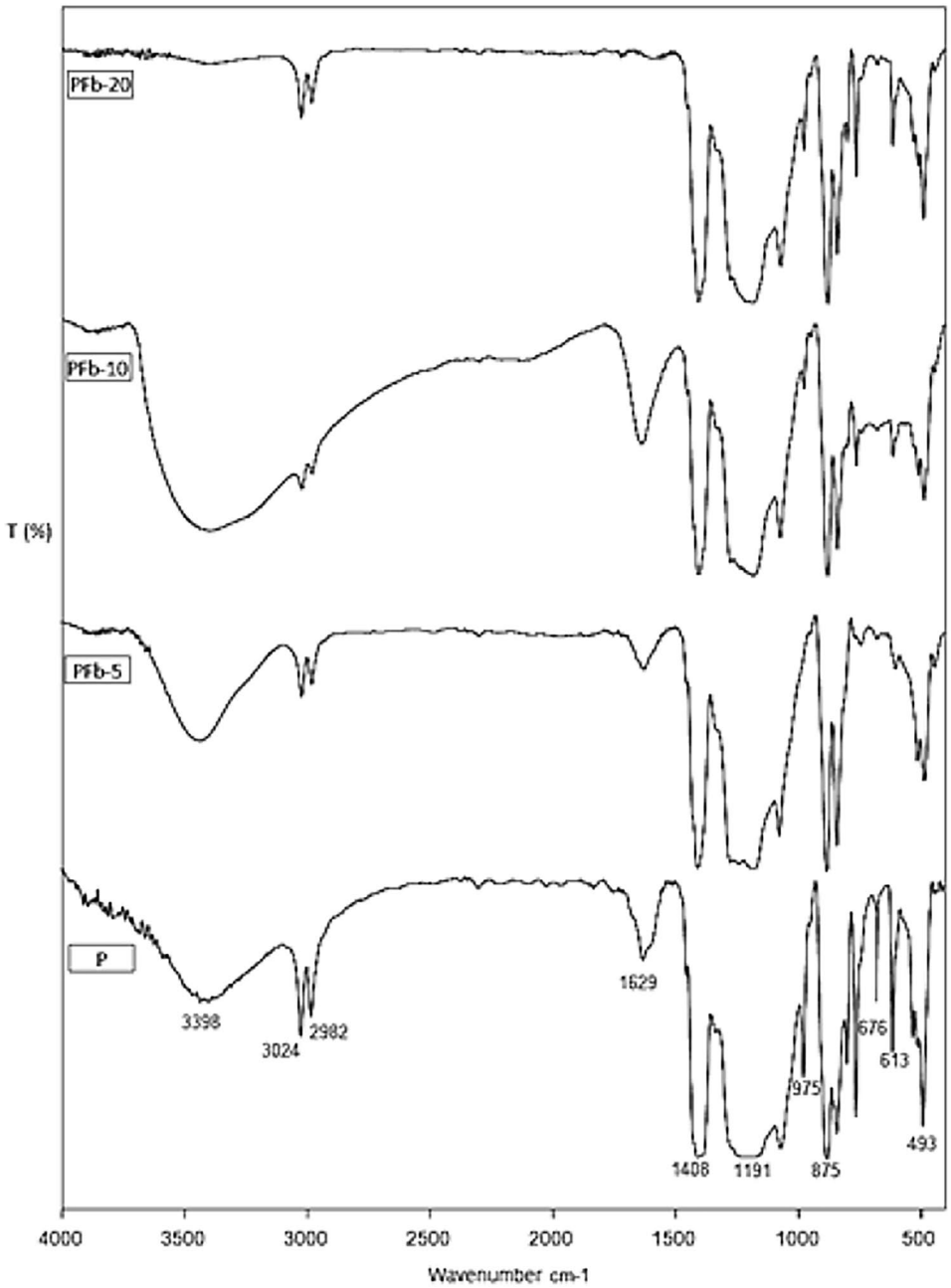

Fig. 5 FT-IR spectrums of P and PFb composites

the anionic character of MO (Table S1). Thus, it was aimed to comment on the surface charge of the composite in the aqueous medium with the adsorption behavior of MO. Since the adsorption and photocatalytic activity will be investigated sequentially, the effect of different acidic areas was excluded. Performance studies were carried out at 25 °C.

Table 1 BET surface area of (S_{BET}) Fb and PFb composites

Sample	S_{BET} (m^2/g)	V_{total} (cm^3/g)	V_{micro} (cm^3/g)	Pore width (nm)	WU%	PO%
Fb	34.33	0.022	0.000895	5.4	-	-
P	4.11	0.042	0.000554	6.3	57.2	65.5
PFb-5	4.1	0.008	0.000144	5.5	51.7	56.0
PFb-10	12.35	0.013	0.000381	5.4	66.5	76.6
PFb-20	8.02	0.025	0.000082	5.7	55.3	63.1

Controlled cooling was done to keep the ambient temperature at a constant value. MO adsorption of composite was checked by analyzing the samples in UV spectrophotometer taken at regular intervals. Then, the mixture was exposed to UV light of 30 W, 254 nm wavelength in air circulation for 30 min. At the end of the 30th min, 0.01 mol/L H_2O_2 was added to the solution, and UV treatment was carried out for 5 more minutes under the same conditions. Thus, the dye removal performances were investigated in adsorption and photocatalytic systems in the presence of air and peroxide.

Removal of dyestuffs by adsorbing on various adsorbents is one of the most frequently used methods. The cost, efficiency, applicability, and reuse of the adsorbent are the parameters that directly affect the process efficiency and material selection. Polymeric composites can be used as adsorbent in the batch system. Those are the main components for the filtration process. The dye removal efficiencies of composites are investigated in batch environments in this study; however, those are promising candidates for filtration system [32].

The biggest drawback of removing various impurities by adsorbing on the surface is the accumulation of particles and decreasing in efficiency. The separation of these impurities beyond adsorption on the surface is necessary for the continuity of pollution removal. Structures that can be induced by the light radiation and catalyze the pollution have gained importance. Such composites are more advantageous than the known surface deposition method thanks to their self-cleaning feature.

Adsorption and photocatalytic sensitivities of Fb-P composites were investigated sequentially. Photocatalytic tests were carried out using a neutral MO solution and 0.3 g of composite, at 25 °C, under basic conditions consisting of air for 30 min and H_2O_2 for 5 min (Fig. 6).

MO adsorption of Fb-P composites resulted in increased MO adsorption compared to raw P. The incorporation of Fb into the P structure improved the pore structure, pore volume, and functional groups of the composite. However, the structural changes caused by the increasing additive ratio were also effective on the adsorption efficiency. The best MO removal percentage was recorded with PFb-10 as 97.41%. This value proves that PFb-10 has the best pore structure distribution. Increasing the additive ratio to 20% caused the shrinkage of the structure, so the MO adsorption decreased. When considering the MO removal performance and characterization results of powder Fb together, it is known that Fb has small pores and low MO adsorption [25]. Therefore, the removal of MO by PFb composites was not solely due to Fb anchoring. The increased pore structure and functional groups created by Fb addition were effective in increasing the dye adsorption efficiency for PFb composites. Higher adsorption efficiency of PFb-10 than PFb-20 proves that the most suitable structure can be obtained by adjusting the additive amount. Adsorption data and initial MO concentration were applied to Langmuir and Freundlich isotherms to better understand the adsorption mechanism [33], where C_e (mg/L) is the MO concentration in the aqueous solution after adsorption, Q_{max} is max monolayer adsorption capacity of sorbent, and K_f, n, and K_L are the constants of Langmuir and Freundlich isotherm models respectively (Table S2). From the

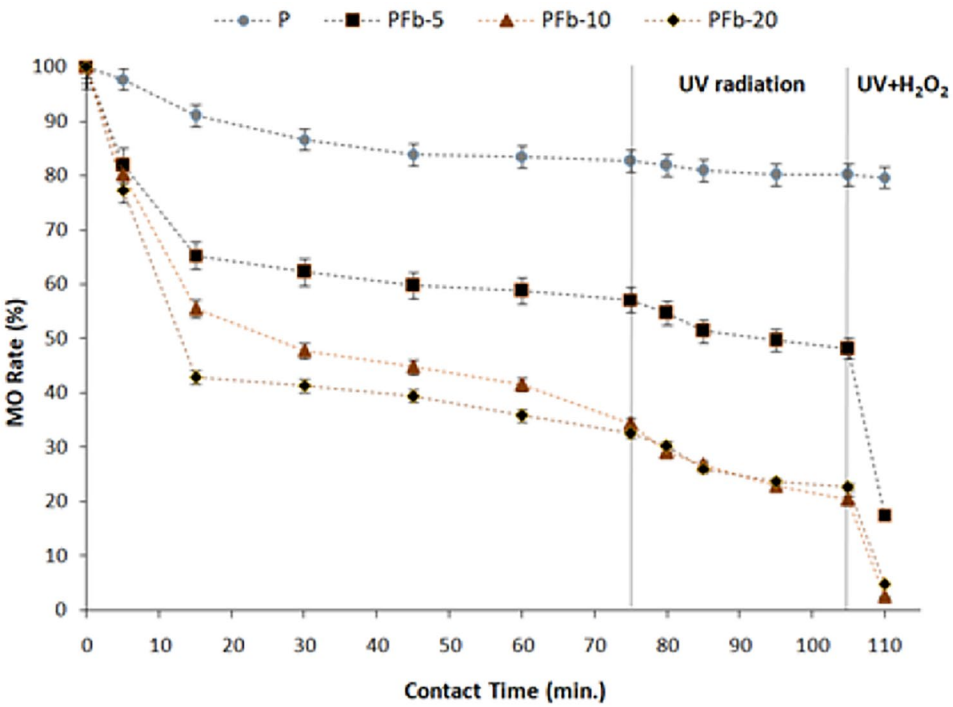

Fig. 6 MO removal (%) performances of composites (adsorbent dosage: 0.3 g, dye concentration and volume:75 mg/L and 50 mL, pH: 7.0, temperature: 298 K, 30 W UV radiation for 30 min (after 75th min), and 30 W UV radiation for 5 min with 0.01 mol/L (after 105th min)

consistency of the graphics, information about the surface homogeneity and the layer of adsorption can be obtained. From the adsorption parameters of the Langmuir model (Table 1), it can be explained that MO adsorption on PFb-5 and PFb-10 takes place with a monolayer arrangement on a homogeneous surface. Besides, MO adsorption on PFb composites were also found to fit the Freundlich model (Fig. S9). These data are compatible with the surface properties of composites because the Fb additive in PVDF composites increased the structure roughness and structural difference. Therefore, multilayer MO adsorption on the heterogeneous surface is likely to have taken place. The lamellar adhesion increased with an increased Fb ratio directly proportional to the electrostatic attraction force. Although the adsorption capacity of PFb-20 is less than other composites, its compliance with the Freundlich model is remarkable. That is an indication for increased electrostatic effect with increasing Fb ratio.

The maximum adsorption capacity of 31.44 mg/g for PFb-20 was calculated at different initial concentrations. Considering the additive rate and removal% values in the composite structure, the calculated values are quite reasonable because the total performance of powder Fb inside the composite is prevented due to the interaction of Fb with the polymer. However, the MO removal of PFb composites increased by approximately 79.1% compared to those obtained by P. The maximum Langmuir value for congo red adsorption on polyaniline-zinc titanate (PANI/ZTO) nanocomposite was calculated as 64.51 mg/g [34–36].

Photocatalytic activity

It was considering the photosensitivity of Fb that the composites containing Fb might also be sensitive to photonic excitation. The photocatalytic activities of PFb composites were investigated. The MO adsorption behaviors of samples were examined for 75 min and those were exposed to UV irradiation in the presence of 0.01 mol/L H_2O_2 for 5 min. After that, composites were exposed to UV for 30 min in air circulation under the same conditions. MO removal% values are given in Fig. 6 with experimental conditions. It is understood that the contact time of 60 min is sufficient for the adsorption equilibrium. With the UV radiation, MO amount decreased for all composites due to photocatalytic effect. Sequential adsorption and photocatalyst is the clear indicator for the activity of UV-induced functional groups. Iron derivatives in the Fb structure were stimulated by ultraviolet absorption and those performed activity in MO removal [37]. There was no change in MO concentration with UV treatment in control samples of P containing and pure MO solution. It is understood that there is no significant relation between MO removal and Fb content of the composites. The efficiency of PFb-10 is close to that of PFb-20 but about 1.5 times the efficiency of PFb-5 (2 times the theoretically expected). With the increase in Fb content, the excited electron and hole formation increases and higher photocatalytic activity is expected. However, Fb fixed composite structure limits the theoretical expectation. The difference in activity between PFb-5 and PFb-10 is a good example for this. The less suppressed the structure, the higher the rate of penetration of the substrate and the greater the exposure to radiation. With the excitation of the valance band electron, a conduction band electron (e^-) and a valance gap (h^+) electron–hole pair are formed. Radicals formed as a result of the interaction of these structures with oxide, hydroxide, or peroxide derivatives degrade the pollution [38].

Induction of radical formation through iron derivatives proceeds over electron–hole pair is called the photo-Fenton process and is shown as Eqs. 3–8 [39].

$$PFb + h\nu \rightarrow e^- + h^+ \quad (3)$$

$$Fe^{2+} + H_2O_2 \rightarrow Fe^{3+} + {}^{\bullet}OH + OH^- \quad (4)$$

$$H_2O + h^+ \rightarrow {}^{\bullet}OH + H^+ \quad (5)$$

$$O_2 + e^- \rightarrow O_2^{-\bullet} \quad (6)$$

$$H_2O_2 + h\nu \rightarrow 2{}^{\bullet}OH \quad (7)$$

$${}^{\bullet}OH + dye \rightarrow dye_{ox} \quad (8)$$

After the adsorption equilibrium is reached, it is understood that some radical species are formed in the presence of oxidizer and UV radiation. The significant effect of radicals is directly related to the e^-/h^+ recombination

Table 2 Ads parameters: isotherm and pseudo-first-order kinetic parameters of P and PFb for MO adsorption

	Langmuir isotherm			Freundlich isotherm		Pseudo-first-order kinetic				
	Q_{max} (mg/g)	K_L (L/mg)	R^2	K_f ($mg^{1-n}/g\ L^n$)	1/n	R^2	$Q_{e.exp}$	k_1	$Q_{e.cal}$	R^2
P	5.988	0.0667	0.9822	0.4789	0.6403	0.9819	2.8277	0.0832	2.8274	0.9622
PFb-5	12.019	0.0338	0.9824	0.6332	0.637	0.9769	6.994	0.225	7.080	0.8496
PFb-10	23.8	0.0176	0.9874	0.857	0.627	0.9813	9.678	0.779	10.965	0.846
PFb-20	31.44	0.0138	0.9559	0.795	0.69	0.9739	10.646	0.298	10.688	0.988

rate, the amount of e^-/h^+, and the types of conduction and valence bands in which these e^-/h^+s accumulate. Another factor affecting the photocatalysis efficiency is the dissolved organic/inorganic ions in the waste water. These structures generally scavenge photocatalysis by changing the surface properties of the parent catalyst or the reaction pathway. Sulfate, chloride, ascorbic acid, and bicarbonate ions have high adsorbing capacity and affect photocatalysis by causing the surface charge to become negative [40]. In this study, methanol (MeOH) and tert-butyl-alcohol (TBA) were tested as scavenging agents. Rate constants for SO_4.- and OH of MeOH and TBA are $k_{SO4.-} = 1.6 \times 10^{*}7\ M^{-1}\ s^{-1}$, $k_{OH.-} = 1.9 \times 10^{*}9\ M^{-1}\ s^{-1}$ and $k_{SO4.-} = 4.0 \times 10^{*}5$ M, respectively. $k_{OH.-} = 6.0 \times 10^{*}8\ M^{-1}\ s^{-1}$, while MeOH quenches SO_4.- and OH.-, TBA is only HO. It is effective in quench [41]. As shown in Fig. S10, a significant decrease in MO removal was noted when both MeOH and TBA were added. The MO removal rate, which was 93.4% under the stated conditions, was recorded as 51.4% with 57.8 TBA in the presence of MeOH. These results proved the significant efficiency of OH radicals in the catalysis process. The absence of SO_4.- radicals increases the efficiency of MeOH and HO. The quenching rate increased [42]. The cavities formed by the excitation of iron derivatives on the membrane surface interact with the peroxide and form hydroxide radicals. It has been understood from the control experiments that the formation of HO by beam activation of peroxide in the absence of a catalyst is negligible. Similarly, in the presence of oxygen, radical formation is at a very low level compared to the peroxide environment. In addition, the quenching of SO_4 by MeOH in advanced oxidation processes in which persulfate is used shows the presence of radicals originating from S_2O_8 in the reaction mechanism [43]. For a better understanding of the MO removal mechanism, IR spectra of the composites after MO adsorption, UV, and UV + H_2O_2 exposure are shown in Figs. S11–13. Unlike the bare IR spectrums of PFb composites (Fig. 5), it is understood that the band observed at 1748 cm^{-1} belongs to the carbonyl derivatives formed by the interaction of the MO-PVDF chain. While this band was quite evident in the MO-adsorbed PFb-10 sample, its intensity decreased in UV and UV-H_2O_2 applications. Therefore, the radicals formed in the presence of light and peroxide also had an effect on the MO derivatives attached to the surface. After adsorption and photocatalysis, changes in some characteristic bands of the composite such as 976, 613 cm^{-1} indicate that the crystal structure has turned amorphous. It was understood that PFb-5 gave a higher yield compared to the other composites, since the radicals enter the pores easily, as well as the ease of entry of the substrate. Different oxygen sources have been used to better understand the photocatalytic effect. Since the solubility of H_2O_2 in water, it diffused immediately in active areas, and a 30.6% increase was observed in the MO removal of PFb-5 in presence of H_2O_2 compared with oxygen environment. This value is 17.8% and 17.94% for PFb-10 and PFb-20, respectively. Although the increase in the Fb ratio has the disadvantage of compression, which prevents light and substrate transportation, more radicals are formed at high Fb rates. Within the scope of this study, PFb composites meet the objectives of preparing photocatalytic composites under economic conditions. Catalytic metal–metal oxide and carbon support created a synergistic effect and accelerated electron movement [44].

PFb composites facilitate the use of Fb by preventing the leaching of iron derivatives into the solution and preventing the reaction from getting out of control [45]. The Composite was separated and the solution was continued to UV radiation. There was no change in the MO concentration as a result of UV exposure under the same conditions. MO removal results were applied to pseudo-first-order and pseudo-second-order kinetic models. Highest Q_e value was calculated as 10.965 for the PFb-10 (Table 1). The sudden increase in photocatalytic MO removal with H_2O_2 caused a deviation of kinetic results (Fig. S14).The rate constants calculated for the PFb composites consistent with the literature.

In this study, the MO removal performance of the Fb-doped composites obtained by the economical method is quite satisfactory when compared with the complex and high-cost composite catalyst. PFb composites have the advantage of being easily separated from the environment by magnetic effect (Fig S15). The reusability of dye-saturated composites was investigated after washed in 50 ml 0.5 mol/L HCl for 10 min by stirring. The sample was washed with distilled water until neutral pH and adsorption process was repeated. The performances were calculated in terms of dye removal capacity. After 4 circulations, the average total MO removal efficiency decreased by $4\% \pm 1$. Particles entering the composite pores and the applied radiation were effective for this decrease. The low-cost and high catalytic effect of composites with recyclability, even re-synthesis of composites is an advantageous alternative.

Many studies have been reported on the adsorption and catalytic removal of dye, organic pollution, pesticides, and heavy metals using magnetic biochar-anchored polymeric composites. The preparation conditions, substrate, and the removal efficiency are the evidence of the application's success. Different dye removal studies catalyzed by composites and powders under similar conditions are shared in Table 2 for comparison. Many parameters are important in removal efficiency such as the composition of catalyst, amount and type of substrate, and reaction time. Composite membranes are structures in which the substrate is catalyzed during filtration at a certain flow rate. Membranes prepared by fixing Fe, Ti, and Bi oxides to PVDF showed good filtration and degradation performance. However, they have drawbacks such as very high-cost and harsh test conditions, such as high light power and low substrate concentration. PFb composites are inexpensive and good-performing membrane candidates for

Table 3 Photocatalytic dye removal studies with different adsorbent-photocatalyst

Catalyst-biochar precursor	Amount or surface area (for membranes)	Substrate and amount	Power (W)	Time	Removal mechanism and efficiency	Ref.
ZnO/biochar	100 mg	160 mg/L methylene blue	250	≅200 min	Degradation 95.19%	[46]
TiO_2-biochar	10 mg	20 mg/L methyl orange	500	150 min	Degradation 96.98%	[47]
FCF-pDA-PVDF (Fe-biochar-) composite beads	1.0 g	10 mg/L methyl orange	300	≅75 min	Degradation≅100%	[48]
MIL-53(Fe)/PVDF	4.7 cm diameter	20 ppm of tetracycline	100 W Xe lamp, UV light	30 min	Degradation 93%	[49]
Fe (III)-TiO_2/ PVDF composite membrane	13–5 cm	10 mg/L 250 mL bisphenol-A (BPA)	500 W sunlight Xenon lamp-	180 min	Degradation 69.9%	[50]
TiO2-PVDF-co-HFP matrix	0.10 m×0.15 m	100 mg/L Congo red (CR) and methylene blue (MB)	8 W UV light	4 h	Degradation-cleaning≅100%	[51]
MCU-C3N4/PVDF membrane	(0.22 µm, 47 mm)	5 mg/L rhodamine B (RhB) 5 mg/L tetracycline hydrochloride (TC)	300 W Xe lamp	60 min	Degradation 84.24% 71.26%	[52]
Bi2WO6 @MIL-100(Fe)-PVDF	14.6 cm^2	10 mg/L 100 mL pirimicarb	70 W visible light	240	Degradation 86%	[53]
Fe-CTW (FeCl2-treated waste textile-based) biochar	50 mg	75 mg/L methyl orange	30 W	35 + 10 min	Degradation 87.4%	[25]
P PFb-5 PFb-10 PFb-20	0.3 g	75 mg/L methyl orange	30 W	75 + 30 + 5* min	Removal** 20.35% 82.47% 97.41% 95.23%	This study

*30 W UV radiation for 30 min (after the 75th minute) and 30 W UV radiation for 5 min with 0.01 mol/L (after the 105th minute)

**Total removal by adsorption and degradation

in situ dye filtration and degradation. What distinguishes the PFb composites prepared in this study from the others is the remarkable photocatalytic efficiency (1), its two-step simple preparation method (2), and its low energy requirement (3). Thus, the production of catalytic compositions from cost-free raw materials and protection of the environment against disposal or burning of waste materials were achieved.

Conclusions

Recycling of industrial waste materials provides both environmental protection and cheap raw material supply. Adsorbent-photocatalytic composites were synthesized by facile method in two steps by adding 0, 5, 10, and 20% by mass of waste textile-based biochar (Fb) to PVDF. MO adsorption and photocatalysis on composites characterized by FT-IR, SEM, XRD, TG–DTA, and BET analyses were investigated. It was understood that the composition containing 10% FbPFb-10 had the best pore structure encourage substrate and radical diffusion. The highest MO removal performance were recorded as 97.4% with PFb-10.

The samples were easily separated from the reaction medium by magnet, and their reuse efficiency was investigated. After 4 repetitions, the dye removal efficiency of PFb composites were found as 94% in average. From the TG analysis, it was understood that Fb had a catalytic effect for decomposing the polymer structure.

Magnetic PFb composites prepared by adding waste textile-based Fb to PVDF are an alternative materials as filtration membranes with their low-cost and effective activity. In addition, it provides indirect contribution to reduce environmental pollution. Magnetic PFb composites could be considered as a product of model study aimed waste recycling.

Supplementary Information The online version contains supplementary material available at https://doi.org/10.1007/s00396-023-05177-z.

Author contribution The authors declare that they have no conflicts of interest. All authors contributed to the study conception and design. Material preparation, data collection and analysis were performed by Huseyin Gumus and Bulent Buyukkidan. The first draft of the manuscript was written by Huseyin Gumus and all authors commented on previous versions of the manuscript. All authors read and approved the final manuscript.

Funding This work was financially supported by the Department of Scientific Research Project at the University of Kutahya Dumlupinar with a funding number Kütahya DPU-BAP 2020–08.

Data Availability All datasets were given as raw and interpreted in this study and in the supplementary materials.

Declarations

Competing interests The authors declare no competing interests.

Ethical approval Not applicable.

References

1. Yi Y, Tu G, Zhao D, Tsang PE, Fang Z (2019) Biomass waste components significantly influence the removal of Cr(VI) using magnetic biochar derived from four types of feedstocks and steel pickling waste liquor. Chem Eng J 360:212–220. https://doi.org/10.1016/j.cej.2018.11.205
2. Zhang L, Guo J, Huang X, Wang W, Sun P, Li Y, Han J (2019) Functionalized biochar-supported magnetic MnFe 2 O 4 nanocomposite for the removal of Pb(ii) and Cd(ii). RSC Adv 9:365–376. https://doi.org/10.1039/c8ra09061k
3. Dong X, He L, Hu H, Liu N, Gao S, Piao Y (2018) Removal of 17B-estradiol by using highly adsorptive magnetic biochar nanoparticles from aqueous solution. Chem Eng J 352:371–379. https://doi.org/10.1016/j.cej.2018.07.025
4. Lingamdinne LP, Choi JS, Angaru GKR, Karri RR, Yang JK, Chang YY, Koduru JR (2022) Magnetic-watermelon rinds biochar for uranium-contaminated water treatment using an electromagnetic semi-batch column with removal mechanistic investigations. Chemosphere 286:131776. https://doi.org/10.1016/j.chemosphere.2021.131776
5. Dai SJ, Zhao YC, Niu DJ, Li Q, Chen Y (2019) Preparation and reactivation of magnetic biochar by molten salt method: relevant performance for chlorine-containing pesticides abatement. J Air Waste Manag Assoc 69:58–70. https://doi.org/10.1080/10962247.2018.1510441
6. Wen Q, Chen Y, Rao X, Yang R, Zhao Y, Li J, Xu S, Liang Z (2022) Preparation of magnesium Ferrite-Doped magnetic biochar using potassium ferrate and seawater mineral at low temperature for removal of cationic pollutants. Biores Technol 350:126860. https://doi.org/10.1016/j.biortech.2022.126860
7. Herath A, Navarathna C, Warren S, Perez F, Pittman CU, Mlsna TE (2022) Iron/titanium oxide-biochar (Fe2TiO5/BC): a versatile adsorbent/photocatalyst for aqueous Cr(VI), Pb2+, F- and methylene blue. J Colloid Interface Sci 614:603–616. https://doi.org/10.1016/j.jcis.2022.01.067
8. Pan Y, Peng Z, Liu Z, Shao B, Liang Q, He Q, Wu T, Zhang X, Zhao C, Liu Y, Ge L, He M (2022) Activation of peroxydisulfate by bimetal modified peanut hull-derived porous biochar for the degradation of tetracycline in aqueous solution. J Environ Chem Eng 10:107366. https://doi.org/10.1016/j.jece.2022.107366
9. Welter N, Leichtweis J, Silvestri S, Sánchez PIZ, Mejía ACC, Carissimi E (2022) Preparation of a new green composite based on chitin biochar and ZnFe2O4 for photo-Fenton degradation of Rhodamine B. J Alloy Compd 901:163758. https://doi.org/10.1016/j.jallcom.2022.163758
10. Zahedifar M, Seyedi N, Salajeghe M, Shafiei S (2020) Nanomagnetic biochar dots coated silver NPs (BCDs-Ag/MNPs): a highly efficient catalyst for reduction of organic dyes. Mater Chem Phys 246:122789. https://doi.org/10.1016/j.matchemphys.2020.122789
11. Li W, Chen Y, Yao L, Ren X, Li Y, Deng L (2020) Fe3O4/PVDF-HFP photothermal membrane with in-situ heating for sustainable, stable and efficient pilot-scale solar-driven membrane distillation. Desalination 478:114288. https://doi.org/10.1016/j.desal.2019.114288
12. Huang ZH, Zhang X, Wang YX, Sun JY, Zhang H, Liu WL, Li MP, Ma XH, Xu ZL (2020) Fe3O4/PVDF catalytic membrane treatment organic wastewater with simultaneously improved permeability, catalytic property and anti-fouling. Environ Res 187:109617. https://doi.org/10.1016/j.envres.2020.109617
13. Zhu J, Zhou S, Li M, Xue A, Zhao Y, Peng W, Xing W (2020) PVDF mixed matrix ultrafiltration membrane incorporated with deformed rebar-like Fe3O4–palygorskite nanocomposites to enhance strength and antifouling properties. J Membr Sci Res 612. https://doi.org/10.1016/j.memsci.2020.118467
14. Sun J, Li S, Ran Z, Xiang Y (2020) Preparation of Fe3O4@TiO2 blended PVDF membrane by magnetic coagulation bath and its permeability and pollution resistance. J Market Res 9:4951–4967. https://doi.org/10.1016/j.jmrt.2020.03.014
15. Li H, Jiang D, Huang Z, He K, Zeng G, Chen A, Yuan L, Peng M, Huang T, Chen G (2019) Preparation of silver-nanoparticle-loaded magnetic biochar/poly(dopamine) composite as catalyst for reduction of organic dyes. J Colloid Interface Sci 555:460–469. https://doi.org/10.1016/j.jcis.2019.08.013
16. Berkün Olgun Ö, Palas B, Atalay S, Ersöz G (2021) Photocatalytic oxidation and catalytic wet air oxidation of real pharmaceutical wastewater in the presence of Fe and LaFeO3 doped activated carbon catalysts. Chem Eng Res Des 171:421–432. https://doi.org/10.1016/j.cherd.2021.05.017
17. Chen L, Ren X, Li Y, Hu D, Feng X, Liu Y, Zhao J (2022) High flux Fe/activated carbon membranes for efficient degradation of organic pollutants in water by activating sodium persulfate. Sep Purif Technol 285:120411. https://doi.org/10.1016/j.seppur.2021.120411
18. Thines KR, Abdullah EC, Mubarak NM, Ruthiraan M (2017) Synthesis of magnetic biochar from agricultural waste biomass to enhancing route for waste water and polymer application: a review. Renew Sustain Energy Rev 67:257–276. https://doi.org/10.1016/j.rser.2016.09.057
19. Gumus H, Buyükkidan B (2022) Pollution removal performance of chemically functionalized textile waste biochar anchored poly (vinylidene fluoride) adsorbent, Journal of the Turkish Chemical Society Section A. Chemistry 9:777–792
20. Buonomenna MG, Golemme G, Figoli A, Drioli E (2010) Fluorinated membranes as interfaces for application in catalysis. Desalination 250:1147–1149. https://doi.org/10.1016/j.desal.2009.09.129
21. El-Sayed SA, Mostafa ME (2014) Pyrolysis characteristics and kinetic parameters determination of biomass fuel powders by differential thermal gravimetric analysis (TGA/DTG). Energy Convers Manag 85:165–172. https://doi.org/10.1016/j.enconman.2014.05.068
22. Zazo JA, Bedia J, Fierro CM, Pliego G, Casas JA, Rodriguez JJ (2012) Highly stable Fe on activated carbon catalysts for CWPO upon FeCl3 activation of lignin from black liquors. Catal Today 187:115–121. https://doi.org/10.1016/j.cattod.2011.10.003
23. Gumus H (2020) Catalytic performance of polyvinylidene fluoride (Pvdf) supported tio2 additive at microwave conditions, Journal of the Turkish Chemical Society, Section A. Chemistry 7:361–374. https://doi.org/10.18596/jotcsa.610886
24. Faaliyan K, Abdoos H, Borhani E, Afghahi SSS (2018) Magnetite-silica nanoparticles with core-shell structure: single-step synthesis, characterization and magnetic behavior. J Sol-Gel Sci Technol 88:609–617. https://doi.org/10.1007/s10971-018-4847-z
25. Gumus H, Buyukkidan B (2023) A simple and green preparation route of waste textile based photocatalytic biochars for pollution removal. Chem Afr. https://doi.org/10.1007/s42250-023-00625-3
26. Gaabour LH (2020) Analysis of Spectroscopic, Optical and magnetic behaviour of PVDF/PMMA blend embedded by magnetite (Fe_3O_4) nanoparticles. Opt Photonics J 10:197–209. https://doi.org/10.4236/opj.2020.108021
27. Gumus H (2019) Performance investigation of Fe 3 O 4 blended poly (vinylidene fluoride) membrane on filtration and benzyl alcohol

oxidation: evaluation of sufficiency for catalytic reactors. Chin J Chem Eng 27:314–321. https://doi.org/10.1016/j.cjche.2018.05.006
28. Xin T, Ma M, Zhang H, Gu J, Wang S, Liu M, Zhang Q (2014) A facile approach for the synthesis of magnetic separable Fe3O4@TiO2, core–shell nanocomposites as highly recyclable photocatalysts. Appl Surf Sci 288:51–59. https://doi.org/10.1016/j.apsusc.2013.09.108
29. O-Rak K, Phakdeepataraphan E, Bunnak N, Ummartyotin S, Sain M, Manuspiya H (2014) Development of bacterial cellulose and poly(vinylidene fluoride) binary blend system: Structure and properties. Chem Eng J 237396–402. https://doi.org/10.1016/j.cej.2013.10.032
30. Ali MA (2014) Synthesis of pyranopyrazoles using magnetic Fe3O4 nanoparticles as efficient and reusable catalyst. Tetrahedron. https://doi.org/10.1016/j.tet.2014.03.024
31. Choi GG, Jung SH, Oh SJ, Kim JS (2014) Total utilization of waste tire rubber through pyrolysis to obtain oils and CO2 activation of pyrolysis char. Fuel Process Technol 123:57–64. https://doi.org/10.1016/j.fuproc.2014.02.007
32. Komaraiah D, Radha E, Sivakumar J, Ramana Reddy MV, Sayanna R (2020) Photoluminescence and photocatalytic activity of spin coated Ag+ doped anatase TiO2 thin films. Opt Mater 108. https://doi.org/10.1016/j.optmat.2020.110401
33. Silva TL, Cazetta AL, Souza PSC, Zhang T, Asefa T, Almeida VC (2018) Mesoporous activated carbon fibers synthesized from denim fabric waste: efficient adsorbents for removal of textile dye from aqueous solutions. J Clean Prod 171:482–490. https://doi.org/10.1016/j.jclepro.2017.10.034
34. Bhat SA, Zafar F, Mirza AU, Mondal AH, Kareem A, Haq QM, Nishat N (2020) NiO nanoparticle doped-PVA-MF polymer nanocomposites: preparation, Congo red dye adsorption and antibacterial activity. Arab J Chem 13:5724–5739. https://doi.org/10.1016/j.arabjc.2020.04.011
35. Singh S, Perween S, Ranjan A (2021) Dramatic enhancement in adsorption of congo red dye in polymer-nanoparticle composite of polyaniline-zinc titanate. J Environ Chem Eng 9:105149. https://doi.org/10.1016/j.jece.2021.105149
36. Raj RM, Ganesan S, Suganthi S, Vignesh S, Hatamleh AA, Alnafisi BK, Venkatesan R, Raj V, Lo H-M (2023) Facile construction of cost-effective zinc-aluminium polymeric framework for efficient removal of selective both drug and dye from an aqueous medium. Chemosphere 311:137105. https://doi.org/10.1016/j.chemosphere.2022.137105
37. Ye Z, Chen L, Chen H, Han L, Chen Q, Wang D (2018) A-Zirconium phosphate nanocrystals with various morphology for photocatalysis. Chem Phys Lett 709:96–102. https://doi.org/10.1016/j.cplett.2018.08.046
38. Devi LG, Kavitha R (2016) A review on plasmonic metal-TiO 2 composite for generation, trapping, storing and dynamic vectorial transfer of photogenerated electrons across the Schottky junction in a photocatalytic system. Appl Surf Sci 360:601–622. https://doi.org/10.1016/j.apsusc.2015.11.016
39. Gou Y, Chen P, Yang L, Li S, Peng L, Song S, Xu Y (2021) Degradation of fluoroquinolones in homogeneous and heterogeneous photo-Fenton processes: a review. Chemosphere. https://doi.org/10.1016/j.chemosphere.2020.129481
40. Sheng H, Li Q, Ma W, Ji H, Chen Ch, Zhao J (2013) Photocatalytic degradation of organic pollutants on surface anionized TiO2: common effect of anions for high hole-availability by water. Appl Catal B 138–139:212–218
41. Xiao R, He L, Luo Z, Spinney R, Wei Z, Dionysiou DD, Zhao F (2020) An experimental and theoretical study on the degradation of clonidine by hydroxyl and sulfate radicals. Sci Total Environ 710:136333. https://doi.org/10.1016/j.scitotenv.2019.136333
42. Xue Y, Kamali M, Yu X, AppelsL Dewil R (2023) Novel CuO/Cu2(V2O7)/V2O5 composite membrane as an efficient catalyst for the activation of persulfate toward ciprofloxacin degradation. Chem Eng J 455:140201. https://doi.org/10.1016/j.cej.2022.140201
43. Xue Y, Guo Y, Zhang X, Kamali M, Aminabhavi TM, Appels L, Dewil R (2022) Efficient adsorptive removal of ciprofloxacin and carbamazepine using modified pinewood biochar – a kinetic, mechanistic study. Chem Eng J 450:137896. https://doi.org/10.1016/j.cej.2022.137896
44. Zhang H, Zhang C, Zhang Y, Cui P, Zhang Y, Wang L, Wang H, Gao Y (2019) P/N co-doped carbon derived from cellulose: a metal-free photothermal catalyst for transfer hydrogenation of nitroarenes. Appl Surf Sci 487:616–624. https://doi.org/10.1016/j.apsusc.2019.05.144
45. Yang NQ, Li J, Wang YN, Ma J (2021) Investigation of photocatalytic properties based on Fe and Ce Co-doped ZnO via hydrothermal method and first principles. Mater Sci Semicond Process 131:105835. https://doi.org/10.1016/j.mssp.2021.105835
46. Yu F, Tian F, Zou H, Ye Z, Peng C, Huang J (2021) ZnO / biochar nanocomposites via solvent free ball milling for enhanced adsorption and photocatalytic degradation of methylene blue. J Hazard Mater 415:125511. https://doi.org/10.1016/j.jhazmat.2021.125511
47. Aichour A, Zaghouane-Boudiaf H, Khodja HD (2022) Highly removal of anionic dye from aqueous medium using a promising biochar derived from date palm petioles: Characterization, adsorption properties and reuse studies. Arab J Chem 15:103542. https://doi.org/10.1016/j.arabjc.2021.103542
48. Li B, Wang H, Lan Y, Cui Y, Zhang Y, Feng Y, Pan J, Meng M, Wu C (2020) A controllable floating pDA-PVDF bead for enhanced decomposition of H2O2 and degradation of dyes. Chem Eng J 385:123907. https://doi.org/10.1016/j.cej.2019.123907
49. Wu CJ, Maggay IV, Chiang CH, Chen W, Chang Y, Hu C, Venault A (2023) Removal of tetracycline by a photocatalytic membrane reactor with MIL-53(Fe)/PVDF mixed-matrix membrane. J Chem Eng 451:138990. https://doi.org/10.1016/j.cej.2022.138990
50. Yang C, Wang P, Li J, Wang Q, Xu P, You S, Zheng Q, Zhang G (2021) Photocatalytic PVDF ultrafiltration membrane blended with visible-light responsive Fe(III)-TiO2 catalyst: Degradation kinetics, catalytic performance and reusability. Chem Eng J 417:129340. https://doi.org/10.1016/j.cej.2021.129340
51. Yadav A, Sharma P, Panda AB, Shahi VK (2021) Photocatalytic TiO2 incorporated PVDF-co-HFP UV-cleaning mixed matrix membranes for effective removal of dyes from synthetic wastewater system via membrane distillation. J Environ Chem Eng 9:105904. https://doi.org/10.1016/j.jece.2021.105904
52. Huang J, Hu J, Shi Y, Zeng G, Cheng W, Yu H, Gu Y, Shi L, Yi K (2019) Evaluation of self-cleaning and photocatalytic properties of modified g-C 3 N 4 based PVDF membranes driven by visible light. J Colloid Interface Sci 541:356–366. https://doi.org/10.1016/j.jcis.2019.01.105
53. Krishnan SAG, Sasikumar B, Arthanareeswaran G, László Z, Nascimben Santos E, Veréb G, Kertész S (2022) Surface-initiated polymerization of PVDF membrane using amine and bismuth tungstate (BWO) modified MIL-100(Fe) nanofillers for pesticide photodegradation. Chemosphere 304. https://doi.org/10.1016/j.chemosphere.2022.135286